ACS APPLIED MATERIALS & INTERFACES

www.acsami.org Research Article

Hot Electron Driven Photocatalysis on Plasmon-Resonant Grating Nanostructures

Yu Wang, Indu Aravind, Zhi Cai, Lang Shen, George N. Gibson, Jihan Chen, Bo Wang, Haotian Shi, Boxiang Song, Ernest Guignon, Nathaniel C. Cady, William D. Page, Arturo Pilar, and Stephen B. Cronin*

Cite This: *ACS Appl. Mater. Interfaces* 2020, 12, 17459−17465 Read Online

ABSTRACT: We demonstrate the hot electron injection of photoexcited carriers in an Ag-based plasmon resonant grating structure. By varying the incident angle of irradiation, sharp dips are observed in the reflectance with p-polarized light (electric field perpendicular to grating lines) when there is wavevector matching between the incident light and the plasmon resonant modes of the grating and no angle dependence is observed with s-polarized light. This configuration enables us to compare photoelectrochemical current produced by plasmon resonant excitation with that of bulk metal interband absorption simply by rotating the polarization of the incident light while keeping all other parameters of the measurement fixed. With 633 nm light, we observed a 12-fold enhancement in the photocurrent (i.e., reaction rate) between resonant and nonresonant polarizations at incident angles of ±7.6° from normal. At 785 nm irradiation, we observed similar resonant profiles to those obtained with 633 nm wavelength light but with a 44-fold enhancement factor. Using 532 nm light, we observed two resonant peaks (with approximately 10× enhancement) in the photocurrent at 19.4° and 28.0° incident angles, each corresponding to higher order modes in the grating with more nodes per period. The lower enhancement factors observed at shorter wavelengths are attributed to interband transitions, which provide a damping mechanism for the plasmon resonance. Finite difference time domain (FDTD) simulations of these grating structures confirm the resonant profiles observed in the angle-dependent spectra of these gratings and provide a detailed picture of the electric field profiles on and off resonance.

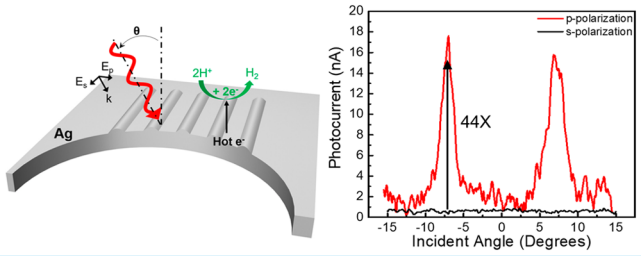

KEYWORDS: *photocatalysis, plasmonic, water splitting, solar fuel, nanostructures*

■ INTRODUCTION

Plasmon resonant enhancement of photocatalytic processes has become a topic of great research interest over the past 10 years. Early studies reported mostly photothermal processes.[1−4] Later studies investigated plasmon enhancement of photoelectrochemical redox processes,[5] such as water splitting, carbon dioxide reduction, and chemical decompsition.[6−16] Liu et al. demonstrated plasmonic enhancement factors of 5× at 532 nm and 66× at 633 nm using Au nanoparticles deposited on TiO_2.[7] Here, Liu et al. integrated strongly plasmonic nanoparticles with strongly catalytic materials (e.g., TiO_2) to drive photocatalytic reactions at an accelerated rate. Since the TiO_2 used in these prior studies had relatively high defect concentration, the mechanism of enhancement was thought to be local field enhancement of sub-band gap defect states.

More recently, there have been several reports of hot electrons in plasmon resonant nanostructures playing an important role in photochemical[17,18] and photoelectrochemical[19,20] processes. Here, photoexcitation of metal nanostructures was used to create populations of hot electrons and hot holes that lie substantially above and below the Fermi energy, presenting the exciting possibility of driving high barrier reactions with visible light. For example, Mukherjee et al. demonstrated dissociation of H_2 by irradiating Au nanoparticles with visible light through a Feshbach resonance with the antibonding state of the hydrogen molecule.[17,18] The Govorov, Atwater, and Nordlander groups have performed detailed calculations of the time evolution of these hot electron distributions in various plasmon resonant nanostructures.[21−25] It is now generally accepted that the relatively narrow distributions of hot electrons and hot holes (separated by ∼2−3 eV) that are initially created with visible light in metal nanostructures decay into a hot Fermi distribution over the time scale of 50−100 fsec through electron−electron

Received: January 2, 2020
Accepted: March 26, 2020
Published: March 26, 2020

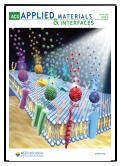

https://dx.doi.org/10.1021/acsami.0c00066
ACS Appl. Mater. Interfaces 2020, 12, 17459−17465

scattering.[26] Ultrafast pump−probe experiments have since revealed that this hot Fermi distribution decays back to equilibrium with the lattice temperature over time scales of several psec.[27,28] In the experiments reported here, we believe that the electrons in this hot Fermi distribution are primarily responsible for producing the photocurrents measured in our photoelectrochemical cell.

Previously, we demonstrated plasmonic amplification with Au gratings and obtained an enhancement factor of 2.3×.[19] This provided a proof-of-principle demonstration that the hot electron can be generated by surface plasmon resonance decay. However, finite difference time domain (FDTD) simulations have predicted that Ag gratings should have sharper and more narrow resonances than Au, as a result of there being fewer interband transitions in the visible wavelength range in Ag as compared with that of Au. Atwater and co-workers showed that hot electrons generated from Au have lower energy than that of hot holes by 1−2 eV, while hot electrons and holes in Ag have equally distributed energy.[22] Besides, Au grating exhibits bandpass resonance in midwave infrared band[29] and narrow resonance in near-infrared band.[30] Ag grating exhibits narrower resonance in visible and near-infrared bands.[31−33] Finally, Ag is commercially much cheaper compared to Au, which has a huge impact for large scale application. In the work presented here, we investigate hot electron driven photochemistry in Ag-based plasmon resonant grating structures at several different wavelengths of excitation. In this study, we present the wavelength dependence of surface plasmon resonance, which shows different resonance modes and diffraction coupling orders at various wavelengths. Additionally, a detailed model mapping the resonant condition and intensity as a function of incident angle and wavelength is also provided. This can be used as a guideline for future surface plasmon resonance (SPR) grating design.

■ RESULTS AND DISCUSSION

Figure 1a shows a scanning electron microscope (SEM) image of the plasmon resonant grating structure used in this work. Here, elemental silicon is covered with 100 nm silicon oxide and patterned by photolithography and reaction ion etching to form a fine corrugated structure with a 500 nm period. A 50 nm Ag film is subsequently deposited on the silicon oxide.[19,34] The structure topography was characterized by atomic force microscopy (Figure S2 in the Supporting Information), showing a peak-to-valley height of 50 nm. Since this is a continuous film grating, the fill factor is 1. A UV−vis reflectance spectrum of this grating structure is shown in Figure 1b. The spectrum was measured by exciting the grating at normal incident (in air) with unpolarized light and collecting light integrated over the full solid angle. Here, we observe two sharp dips in the spectra corresponding to surface plasmon resonant modes at 492 and 604 nm.

In our photoelectrochemical setup, we used an AC lock-in technique in which the incident light is modulated by an optical chopper wheel (Stanford Research Systems SR-540),[19,20,35] and the AC photocurrent was measured using a lock-in amplifier (Stanford Research Systems SR-830), as illustrated in Figure S1 of the Supporting Information. This enablesd us to measure the small photocurrents produced by the relatively short-lived hot electrons in the metal. This AC technique also enabled us to separate the hot electron photocurrent from the DC electrochemical current produced by equilibrated (i.e., cold) electrons. The photoelectrochemical

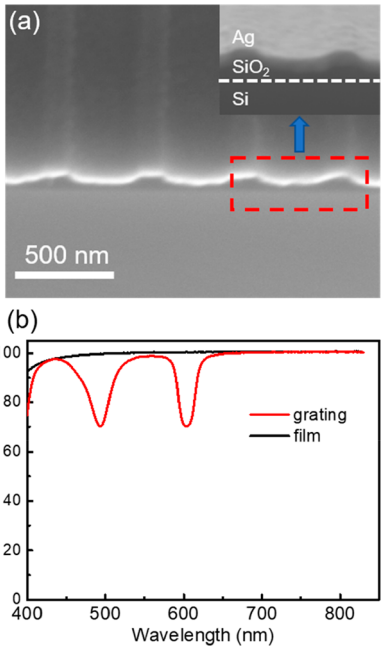

Figure 1. (a) SEM image of the plasmon resonant Ag grating structure. (b) UV−vis diffuse reflectance measurement of Ag grating and Ag film.

measurement was conducted with standard 3-teminal potentiostat (Gamry Inc.) in 0.5 M Na_2SO_4 aqueous solution with the Ag grating as the working electrode, Ag/AgCl (3 M NaCl) as the reference electrode, and a Pt wire as the counter electrode (BASI Inc.). The applied bias with respect to Ag/AgCl was −0.5 V. Copper wires were connected to the top of the Ag gratings by silver paint (SPI Supplies Inc.) in order to exclude the underlying Si substrate from the circuit during the photoelectrochemical measurements. Epoxy resin (DEVCON Inc.) was used to seal the grating on top of a glass slide, exposing only the grating area to the electrolyte.[19,34]

The angle-dependent reflectivity of each grating was calculated using the FDTD method (Lumerical Inc.). The cross-sectional SEM image of the corrugated grating structure (Figure 1a) was imported and fitted to establish the surface profile. The gratings were modeled as custom structure objects with the fitting equations (provided in the Supporting Information) describing the boundaries of the object in Lumerical FDTD solutions. All the simulations were performed with a mesh size of 0.5 nm, and the background medium was water. The gratings were excited by a plane wave source with variable incident angles and polarizations. Bloch boundary conditions were applied on the sides of the gratings to account for the phase change across each period. Perfectly matched layer (PML) boundaries were used along the direction perpendicular to the grating structure. A plane power monitor placed behind the source was used to monitor the reflected power from the gratings, and a 2D field monitor in the plane of the grating was used to record the electric field profile.

Figure 2a shows a schematic diagram illustrating our basic measurement configuration. We achieved resonance by scanning the incident angle of monochromatic light (532, 633, and 785 nm). For the light polarized perpendicular to the lines on the grating (i.e., p-polarized), we observed sharp dips in the photoreflectance (Figure 2b) when there was wave-

https://dx.doi.org/10.1021/acsami.0c00066
ACS Appl. Mater. Interfaces 2020, 12, 17459−17465

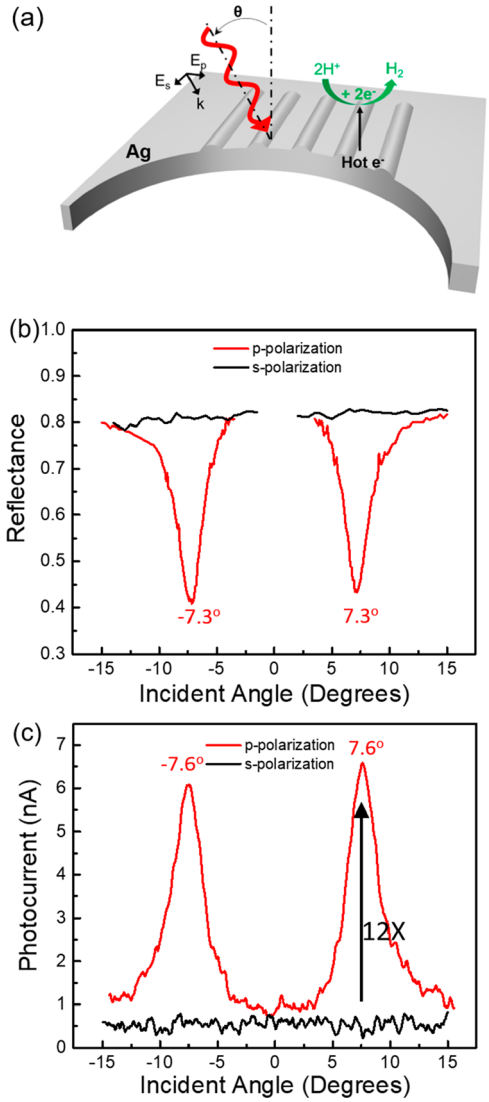

Figure 2. (a) Schematic diagram of the experimental measurement, (b) photoreflectance, and (c) AC photoelectrochemical current measured as a function of incident angle. The red curve corresponds to p-polarized light, and the black curve corresponds to s-polarized light.

vector matching between the incident photons and the plasmon resonant mode. For the experimental Ag-coated grating structure with 633 nm light, this resonance occurs at ±7.3° from normal incidence. For the light polarized parallel to the grating lines (i.e., s-polarization), there is no coupling to the plasmon resonant mode and, consequently, no angle dependence in the photoreflectance. Figure 2c shows the AC photoelectrochemical current under 633 nm illumination. We observed sharp peaks in the AC photocurrent at similar incidence with p-polarized light and no angular dependence with s-polarized light. Here, we were able to achieve a 12-fold increase in photocurrent when exciting on the plasmon resonance, as shown in Figure 2c.

FDTD simulations of these structures were performed to further define the underlying nature of this plasmonic effect (Figure 3). Figure 3a shows the photoreflectance plotted as a function of incident angle for the Ag gratings with 633 nm wavelength light. We observed sharp dips in the photoreflectance at ±7.0°, consistent with our experimental

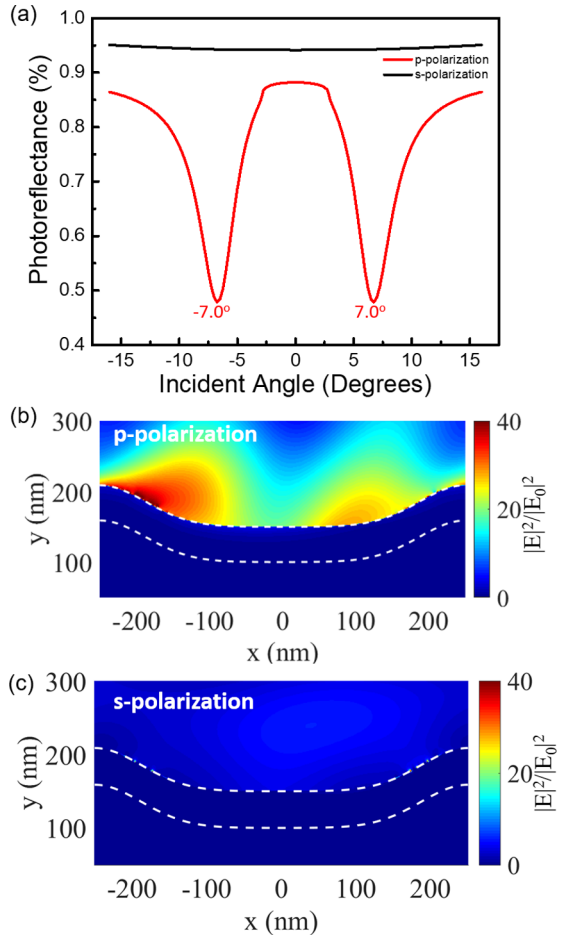

Figure 3. (a) Calculated photoreflectance spectrum of the Ag grating shown in Figure 1a. Electric field distributions taken with (b) resonant and (c) nonresonant polarizations at 7.0° incidence with 633 nm light. The red curve corresponds to p-polarized light, and the black curve corresponds to s-polarized light.

measurements shown in Figure 2b. The electric field strength is plotted along the cross-section of the grating structure in Figure 3b,c. The data in Figure 3b corresponds to resonant excitation at +7.0° incidence with p-polarization, while the data in Figure 3c corresponds to nonresonant excitation at +7.0° incidence with s-polarization. On resonance, we see a plasmon resonant mode with a peak electric field intensity enhancement factor ($|E|^2/|E_0|^2$) of 40× at the metal surface, where E is the electric field at the water-metal interface, and E_0 is the electric field of the incident light.

Figure 4a shows the AC photocurrent measured with 785 nm wavelength illumination. Again, sharp peaks were observed around ±7.1° incidence with p-polarization and no angular dependence was observed with s-polarized light. Here, a plasmonic enhancement factor of 44× was observed in the photocurrent (i.e., hydrogen evolution reaction rate). The corresponding FDTD simulations show similar angle-dependent profiles, as plotted in Figure 4b. It should also be noted that the resonant profiles are narrower at 785 nm than at 633 nm. Larger enhancement factors and narrower resonances observed at longer wavelengths are a result of reduced damping of plasmon resonance, as fewer interband transitions are available at these longer wavelengths. This damping mechanism also explains why smaller enhancement factors were observed with similar gratings made with Au, which has

https://dx.doi.org/10.1021/acsami.0c00066
ACS Appl. Mater. Interfaces 2020, 12, 17459−17465

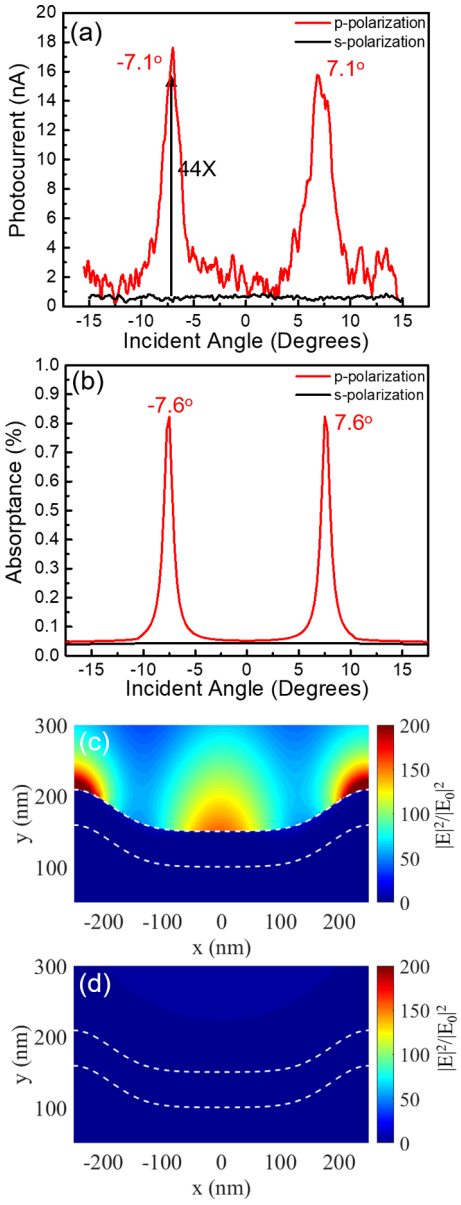

Figure 4. (a) AC photocurrent measured as a function of incident angle and (b) simulated absorptance spectra for 785 nm illumination. (c) Electric field distributions at 7.6° incident angle for (c) p-polarized and (d) s-polarized 785 nm wavelength irradiations.

substantially more interband transitions in the visible wavelength range than Ag. 2D plots of the electric field strength (i.e., $|E|^2$) profiles are plotted in Figure 4c,d. These figures show excitation of a highly symmetric mode (with two nodes per period of the grating) with p-polarization at 785 nm, as compared with the less symmetric mode of Figure 3b. Here, the hottest spot at the water−metal interface has a 200× electric field intensity enhancement factor.

Figure 5a shows the AC photocurrent measured as a function of the incident angle for the same Ag grating taken with 532 nm wavelength light. Here, we observed two resonant peaks at incident angles of ±19.4° and ±28.0° from normal incidence with p-polarized light and no angular dependence with s-polarized light. The calculated absorptance (100% is reflectance) based on FDTD simulations is plotted in Figure 5b and exhibits the same double peak behavior as that plotted in Figure 5a but with resonant angles of ±18.4° and ±28.8°.

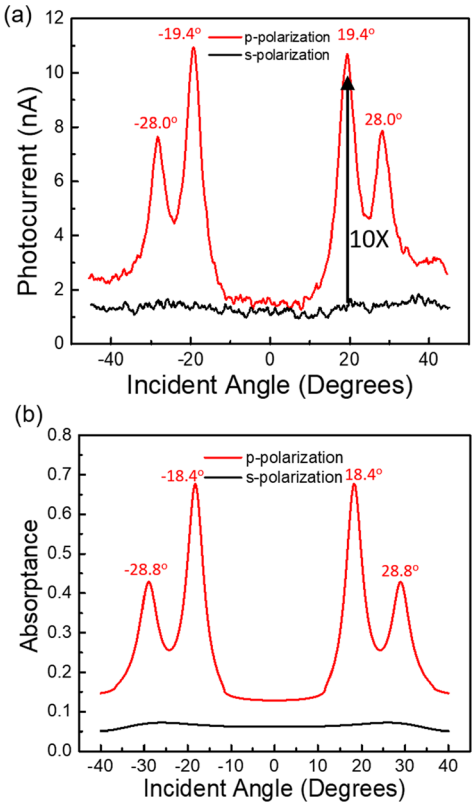

Figure 5. (a) AC photoelectrochemical current measured as a function of incident angle and (b) simulated absorptance spectra for Ag grating with 532 nm irradiation.

The electric field profile calculated on resonance at 18.4° is plotted in Figure 6a and exhibits four nodes in one period of

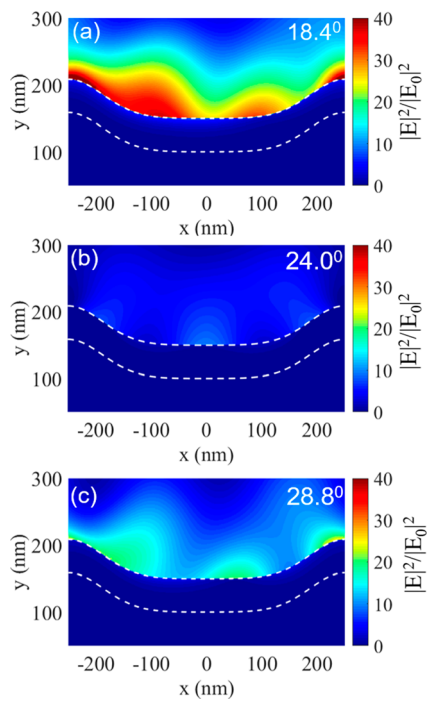

Figure 6. Calculated electric field distributions at (a) 18.4°, (b) 24.0°, and (c) 28.8° incident angles for Ag grating with 532 nm illumination with p-polarization.

https://dx.doi.org/10.1021/acsami.0c00066
ACS Appl. Mater. Interfaces 2020, 12, 17459−17465

the grating. Figure 6c shows the electric field profile of the resonant peak at 28.8°, which exhibits three nodes per period of the grating.

In order to optically excite surface plasmons on diffraction gratings with light polarized perpendicular to the grating lines (i.e., p-polarized), the following condition has to be met:[36,37]

$$\frac{2\pi n_d}{\lambda}\sin\theta + m\frac{2\pi}{P} = -Re\{\beta^{SP}\} \quad (1)$$

where n_d is the dielectric constant of the surrounding water environment, λ is the wavelength of the incident light in vacuum space, P is the period of grating, m is an integer (±1, ±2, etc.) representing the order of diffraction, and β^{SP} represents the surface plasmon wavevector.

$$\beta^{SP} = \beta^{SP_0} + \Delta\beta = \frac{\omega}{c}\sqrt{\frac{\varepsilon_d\varepsilon_{Ag}}{\varepsilon_d + \varepsilon_{Ag}}} + \Delta\beta \quad (2)$$

where β^{SP_0} accounts for the surface plasmon wavevector along the smooth interface between dielectric and Ag metal, $\Delta\beta$ represents the grating presence, ω stands for the angular frequency of incident light, and ε_d and ε_{Ag} mean the dielectric constant of water environment and Ag metal, respectively. For the shallow surface grating like what we used in our experiment, we can neglect $\Delta\beta$ and assume it to be zero. Then, from eqs 1 and 2, we can get:

$$\frac{2\pi n_d}{\lambda}\sin\theta + m\frac{2\pi}{P} = -Re\left\{\frac{\omega}{c}\sqrt{\frac{\varepsilon_d\varepsilon_{Ag}}{\varepsilon_d + \varepsilon_{Ag}}}\right\} \quad (3)$$

Figure 7a shows the calculated resonance condition of the Ag grating for different incident light angles (0°− 40°) and wavelengths (400−900 nm) based on eq 3; Figure 7b shows the simulated absorptance for various incident angles and wavelengths within the same range, and all the calculated resonant angles have been flipped to the positive range. As Figure 7a shows, when the incident light wavelength is from 575−900 nm and incident light angle is between 0° and 40°, only then first diffraction order coupled surface plasmon resonance (m = 1) can be excited, and absorptance in Figure 7b at a resonant angle increased from about 60% to nearly 100% with increasing incident light wavelength. Between 400−575 nm, besides the first diffraction order coupled surface plasmon resonance, there is another second diffraction order coupling (m = 2). The absorptance for second diffraction order coupling is about 10%−20% lower than that of the first diffraction order for the same incident light wavelength. Here, both calculated and simulated results agree very well with our experimental data where we observed a single peak in the absorption for 785 nm incident light having highest absorptance at the resonant angle, which promotes hot electrons and has the highest photocurrent enhancement factor (44×). Besides, 633 nm light incidence also shows a single resonant peak, but it shows it absorbing a lower percentage of light and having a lower photocurrent enhancement factor (12×). At 523 nm, two resonant peaks are seen with one peak having higher enhancement factor than the other.

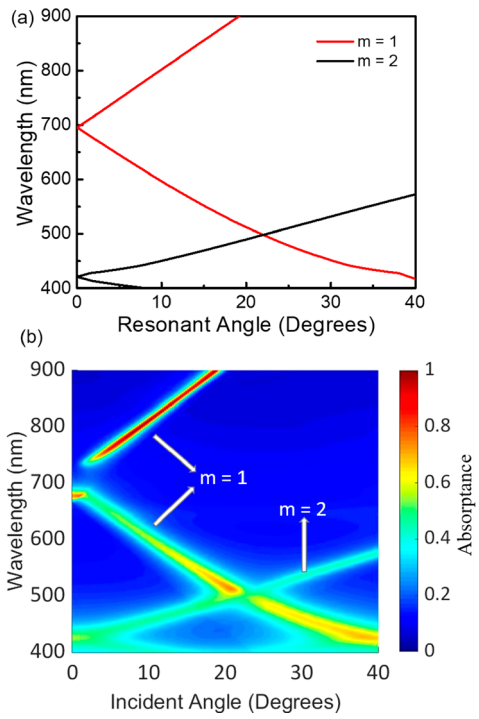

Figure 7. (a) Calculated resonant condition for different incident angles (0°−40°) and incident light wavelengths (400−900 nm). (b) Simulated absorptance spectrum of Ag grating with respect to the incident light wavelength and incident angle.

CONCLUSION

We have presented a spectroscopic approach for studying hot electron driven photocatalysis using a sensitive AC lock-in technique with plasmon resonant grating structures. The incident angle and polarization dependence of these grating structures provide a unique platform for comparing plasmon resonant excitation and bulk interband absorption of metals in photocatalytic processes. As the angle of incident light is tuned through the plasmon resonance with p-polarized light, sharp dips are observed in the photoreflectance and sharp peaks are observed in the photocurrent (i.e., reaction rate). We observe plasmon resonant enhancement factors of 10×, 12×, and 44× at incident wavelengths of 532, 633, and 785 nm, respectively. The lower enhancement factors observed at shorter wavelengths are attributed to interband transitions, which provide a damping mechanism for the plasmon resonance phenomenon. FDTD simulations confirm the angular dependence of the resonant profiles observed experimentally and provide a detailed picture of the electric field profiles of these grating structures for both on and off resonance.

ASSOCIATED CONTENT

Supporting Information

The Supporting Information is available free of charge at https://pubs.acs.org/doi/10.1021/acsami.0c00066.

(Figures of schematic diagrams, AFM images and corresponding surfaces profiles, UV−vis spectra, calculated resonant modes, and simulated absorptance spectra PDF)

AUTHOR INFORMATION

Corresponding Author

Stephen B. Cronin − *Ming Hsieh Department of Electrical Engineering, Department of Chemistry, and Department of Physics and Astronomy, University of Southern California, Los*

https://dx.doi.org/10.1021/acsami.0c00066
ACS Appl. Mater. Interfaces 2020, 12, 17459−17465

Angeles, California 90089, United States; orcid.org/0000-0001-9153-7687; Email: scronin@usc.edu

Authors

Yu Wang − *Mork Family Department of Chemical Engineering and Materials Science, University of Southern California, Los Angeles, California 90089, United States;* orcid.org/0000-0002-0307-1301

Indu Aravind − *Department of Physics and Astronomy, University of Southern California, Los Angeles, California 90089, United States*

Zhi Cai − *Mork Family Department of Chemical Engineering and Materials Science, University of Southern California, Los Angeles, California 90089, United States*

Lang Shen − *Mork Family Department of Chemical Engineering and Materials Science, University of Southern California, Los Angeles, California 90089, United States*

George N. Gibson − *Department of Physics, University of Connecticut, Storrs, Connecticut 06269, United States; Ciencia Inc., East Hartford, Connecticut 06108, United States*

Jihan Chen − *Ming Hsieh Department of Electrical Engineering, University of Southern California, Los Angeles, California 90089, United States;* orcid.org/0000-0001-7065-8287

Bo Wang − *Department of Physics and Astronomy, University of Southern California, Los Angeles, California 90089, United States;* orcid.org/0000-0001-7089-6672

Haotian Shi − *Department of Chemistry, University of Southern California, Los Angeles, California 90089, United States*

Boxiang Song − *Ming Hsieh Department of Electrical Engineering, University of Southern California, Los Angeles, California 90089, United States;* orcid.org/0000-0002-4946-2738

Ernest Guignon − *Ciencia Inc., East Hartford, Connecticut 06108, United States*

Nathaniel C. Cady − *Colleges of Nanoscale Science & Engineering, SUNY Polytechnic Institute, Albany, New York 12203, United States*

William D. Page − *Ciencia Inc., East Hartford, Connecticut 06108, United States*

Arturo Pilar − *Ciencia Inc., East Hartford, Connecticut 06108, United States*

Complete contact information is available at:
https://pubs.acs.org/10.1021/acsami.0c00066

Notes

The authors declare no competing financial interest.

■ ACKNOWLEDGMENTS

This research was supported by the Army Research Office (ARO) Award No. W911NF-17-1-0325 (Y.W.), National Science Foundation (NSF) Award No. CBET-1512505 (L.S.), Air Force Office of Scientific Research (AFOSR) Grant No. FA9550-19-1-0115 (I.A.), Department of Energy (DOE) Award No. DE-SC0019322 (Z.C.), and ACS-PRF Grant #55993-ND5 (J.C.).

■ REFERENCES

(1) Hung, W. H.; Hsu, I. K.; Bushmaker, A.; Kumar, R.; Theiss, J.; Cronin, S. B. Laser Directed Growth of Carbon-Based Nanostructures by Plasmon Resonant Chemical Vapor Deposition. *Nano Lett.* **2008**, *8*, 3278−3282.

(2) Hung, W. H.; Aykol, M.; Valley, D.; Hou, W.; Cronin, S. B. Plasmon Resonant Enhancement of Carbon Monoxide Catalysis. *Nano Lett.* **2010**, *10*, 1314−1318.

(3) Liu, Z.; Hung, W. H.; Aykol, M.; Valley, D.; Cronin, S. B. Optical Manipulation of Plasmonic Nanoparticles, Bubble Formation and Patterning of SERS Aggregates. *Nanotechnology* **2010**, *21*, 105304.

(4) Christopher, P.; Xin, H.; Linic, S. Visible-Light-Enhanced Catalytic Oxidation Reactions on Plasmonic Silver Nanostructures. *Nat. Chem.* **2011**, *3*, 467−472.

(5) Christopher, P.; Xin, H.; Marimuthu, A.; Linic, S. Singular Characteristics and Unique Chemical Bond Activation Mechanisms of Photocatalytic Reactions on Plasmonic Nanostructures. *Nat. Mater.* **2012**, *11*, 1044−1050.

(6) Linic, S.; Christopher, P.; Ingram, D. B. Plasmonic-Metal Nanostructures for Efficient Conversion of Solar to Chemical Energy. *Nat. Mater.* **2011**, *10*, 911−921.

(7) Liu, Z.; Hou, W.; Pavaskar, P.; Aykol, M.; Cronin, S. B. Plasmon Resonant Enhancement of Photocatalytic Water Splitting Under Visible Illumination. *Nano Lett.* **2011**, *11*, 1111−1116.

(8) Hou, W.; Liu, Z.; Pavaskar, P.; Hung, W. H.; Cronin, S. B. Plasmonic Enhancement of Photocatalytic Decomposition of Methyl Orange Under Visible Light. *J. Catal.* **2011**, *277*, 149−153.

(9) Hou, W.; Hung, W. H.; Pavaskar, P.; Goeppert, A.; Aykol, M.; Cronin, S. B. Photocatalytic Conversion of CO_2 to Hydrocarbon Fuels via Plasmon-Enhanced Absorption and Metallic Interband Transitions. *ACS Catal.* **2011**, *1*, 929−936.

(10) Hou, W.; Cronin, S. B. A Review of Surface Plasmon Resonance-Enhanced Photocatalysis. *Adv. Funct. Mater.* **2013**, *23*, 1612−1619.

(11) Lee, S.-M.; Li, W.; Dhar, P.; Malyk, S.; Wang, Y.; Lee, W.; Benderskii, A.; Yoon, J. High-Performance Flexible Nanostructured Silicon Solar Modules with Plasmonically Engineered Upconversion Medium. *Adv. Energy Mater.* **2015**, *5*, 5.

(12) Chen, J.; Bailey, C. S.; Hong, Y.; Wang, L.; Cai, Z.; Shen, L.; Hou, B.; Wang, Y.; Shi, H.; Sambur, J.; Ren, W.; Pop, E.; Cronin, S. B. Plasmon-Resonant Enhancement of Photocatalysis on Monolayer WSe_2. *ACS Photonics* **2019**, *6*, 787−792.

(13) Liu, F.; Song, B.; Su, G.; Liang, O.; Zhan, P.; Wang, H.; Wu, W.; Xie, Y.; Wang, Z. Sculpting Extreme Electromagnetic Field Enhancement in Free Space for Molecule Sensing. *Small* **2018**, *14*, 1801146.

(14) Song, B.; Yao, Y.; Groenewald, R. E.; Wang, Y.; Liu, H.; Wang, Y.; Li, Y.; Liu, F.; Cronin, S. B.; Schwartzberg, A. M. Probing Gap Plasmons Down to Subnanometer Scales Using Collapsible Nanofingers. *ACS Nano* **2017**, *11*, 5836−5843.

(15) Chen, H.; Lee, S.-M.; Montenegro, A.; Kang, D.; Gai, B.; Lim, H.; Dutta, C.; He, W.; Lee, M. L.; Benderskii, A. Plasmonically Enhanced Spectral Upconversion for Improved Performance of GaAs Solar Cells under Nonconcentrated Solar Illumination. *ACS Photonics* **2018**, *5*, 4289−4295.

(16) Chae, H. U.; Ahsan, R.; Lin, Q.; Sarkar, D.; Rezaeifar, F.; Cronin, S. B.; Kapadia, R. High Quantum Efficiency Hot Electron Electrochemistry. *Nano Lett.* **2019**, *19*, 6227−6234.

(17) Mukherjee, S.; Libisch, F.; Large, N.; Neumann, O.; Brown, L. V.; Cheng, J.; Lassiter, J. B.; Carter, E. A.; Nordlander, P.; Halas, N. J. Hot Electrons Do the Impossible: Plasmon-Induced Dissociation of H_2 on Au. *Nano Lett.* **2013**, *13*, 240−247.

(18) Mukherjee, S.; Zhou, L.; Goodman, A. M.; Large, N.; Ayala-Orozco, C.; Zhang, Y.; Nordlander, P.; Halas, N. J. Hot-Electron-Induced Dissociation of H_2 on Gold Nanoparticles Supported on SiO_2. *J. Am. Chem. Soc.* **2014**, *136*, 64−67.

(19) Shen, L.; Gibson, G. N.; Poudel, N.; Hou, B.; Chen, J.; Shi, H.; Guignon, E.; Cady, N. C.; Page, W. D.; Pilar, A.; Cronin, S. B. Plasmon Resonant Amplification of Hot Electron-Driven Photocatalysis. *Appl. Phys. Lett.* **2018**, *113*, 113104.

(20) Hou, B.; Shen, L.; Shi, H.; Kapadia, R.; Cronin, S. B. Hot Electron-Driven Photocatalytic Water Splitting. *Phys. Chem. Chem. Phys.* **2017**, *19*, 2877−2881.

(21) Govorov, A. O.; Zhang, H.; Gun'ko, Y. K. Theory of Photoinjection of Hot Plasmonic Carriers from Metal Nanostructures into Semiconductors and Surface Molecules. *J. Phys. Chem. C* **2013**, *117*, 16616−16631.
(22) Sundararaman, R.; Narang, P.; Jermyn, A. S.; Goddard, W. A., 3rd; Atwater, H. A. Theoretical Predictions for Hot-Carrier Generation from Surface Plasmon Decay. *Nat. Commun.* **2014**, *5*, 5788.
(23) Brown, A. M.; Sundararaman, R.; Narang, P.; Goddard, W. A., 3rd; Atwater, H. A. Nonradiative Plasmon Decay and Hot Carrier Dynamics: Effects of Phonons, Surfaces, and Geometry. *ACS Nano* **2016**, *10*, 957−966.
(24) Narang, P.; Sundararaman, R.; Atwater, H. A. Plasmonic Hot Carrier Dynamics in Solid-State and Chemical Systems for Energy Conversion. *Nanophotonics* **2016**, *5*, 96−111.
(25) Zheng, B. Y.; Zhao, H.; Manjavacas, A.; McClain, M.; Nordlander, P.; Halas, N. J. Distinguishing Between Plasmon-Induced and Photoexcited Carriers in a Device Geometry. *Nat. Commun.* **2015**, *6*, 7797.
(26) Aizpurua, J.; Baumberg, J.; Boltasseva, A.; Christopher, P.; Cortes, E.; Cronin, S. B.; Dadhich, B. K.; de Nijs, B.; Deshpande, P.; Diaz Fernandez, Y.; Fabris, L.; Gawinkowski, S.; Govorov, A.; Halas, N.; Huang, J.; Jankiewicz, B.; Kamarudheen, R.; Khurgin, J.; Lee, T. K.; Mahin, J.; Marini, A.; Maurer, R. J.; Mueller, N. S.; Park, J. Y.; Rahaman, M.; Schlucker, S.; Schultz, Z.; Sivan, Y.; Tagliabue, G.; Thangamuthu, M.; Xu, H.; Zayats, A. New Materials For Hot Electron Generation: General Discussion. *Faraday Discuss.* **2019**, *214*, 365−386.
(27) Wang, Y.; Shen, L.; Wang, Y.; Hou, B.; Gibson, G. N.; Poudel, N.; Chen, J.; Shi, H.; Guignon, E.; Cady, N. C.; Page, W. D.; Pilar, A.; Dawlaty, J.; Cronin, S. B. Hot Electron-Driven Photocatalysis and Transient Absorption Spectroscopy in Plasmon Resonant Grating Structures. *Faraday Discuss.* **2019**, *214*, 325−339.
(28) Wang, Y.; Shi, H.; Shen, L.; Wang, Y.; Cronin, S. B.; Dawlaty, J. M. Ultrafast Dynamics of Hot Electrons in Nanostructures: Distinguishing the Influence on Interband and Plasmon Resonances. *ACS Photonics* **2019**, *6*, 2295−2302.
(29) Sakat, E.; Vincent, G.; Ghenuche, P.; Bardou, N.; Collin, S.; Pardo, F.; Pelouard, J.-L.; Haïdar, R. Guided Mode Resonance in Subwavelength Metallodielectric Free-Standing Grating for Bandpass Filtering. *Opt. Lett.* **2011**, *36*, 3054−3056.
(30) Ren, Z.; Sun, Y.; Lin, Z.; Wang, C. Ultra-Narrow Band Perfect Metamaterial Absorber Based on Dielectric-Metal Periodic Configuration. *Opt. Mater.* **2019**, *89*, 308−315.
(31) Ren, Z.; Sun, Y.; Zhang, S.; Lin, Z.; Wang, C. Tunable Narrow Band Perfect Metamaterial Absorber Based on Guided-Mode Resonance. *Mod. Phys. Lett. B* **2019**, *33*, 1950171.
(32) Ren, Z.; Sun, Y.; Zhang, S.; Zhang, K.; Hu, J.; Lin, Z. Active Optical Switches Based on Polarization-Tuned Guided-Mode Resonance Filters for Optical Communication. *Opt. Commun.* **2018**, *426*, 383−387.
(33) Ren, Z.; Sun, Y.; Zhang, S.; Zhang, K.; Lin, Z.; Wang, S. 2D Non-Polarising Transmission Filters Based on GMR for Optical Communications. *Micro Nano Lett.* **2018**, *13*, 1621−1626.
(34) Shen, L.; Poudel, N.; Gibson, G. N.; Hou, B.; Chen, J.; Shi, H.; Guignon, E.; Page, W. D.; Pilar, A.; Cronin, S. B. Plasmon Resonant Amplification of a Hot Electron-Driven Photodiode. *Nano Res.* **2018**, *11*, 2310−2314.
(35) Sambur, J. B.; Riha, S. C.; Choi, D.; Parkinson, B. A. Influence of Surface Chemistry on the Binding and Electronic Coupling of CdSe Quantum Dots to Single Crystal TiO_2 Surfaces. *Langmuir* **2010**, *26*, 4839−4847.
(36) Homola, J. Electromagnetic Theory of Surface Plasmons. *Surface Plasmon Resonance Based Sensors*; Springer, 2006; pp 3−44.
(37) Roh, S.; Chung, T.; Lee, B. Overview of the Characteristics of Micro-and Nano-Structured Surface Plasmon Resonance Sensors. *Sensors* **2011**, *11*, 1565−1588.

https://dx.doi.org/10.1021/acsami.0c00066
ACS Appl. Mater. Interfaces 2020, 12, 17459−17465